Room-Temperature Mid-Infrared Detection Using Metasurface-Absorber-Integrated Phononic Crystal Oscillator

Zichen Xi, Zengyu Cen, Dongyao Wang, Joseph G. Thomas, Bernadeta R. Srijanto, Ivan I. Kravchenko, Jiawei Zuo, Honghu Liu, Jun Ji, Yizheng Zhu, Yu Yao, and Linbo Shao**

Mid-infrared (MIR) detectors find extensive applications in chemical sensing, spectroscopy, communications, biomedical diagnosis, and space exploration. Alternative to semiconductor MIR photodiodes and bolometers, mechanical-resonator-based MIR detectors show advantages in higher sensitivity and lower noise at room temperature, especially toward longer wavelength infrared. Here, uncooled room-temperature MIR detectors based on lithium niobate surface acoustic wave phononic crystal (PnC) resonators integrated with wavelength-and-polarization-selective metasurface absorber arrays are demonstrated. The detection is based on the resonant frequency shift induced by the local temperature change due to MIR absorptions. The PnC resonator is configured in an oscillating mode, enabling active readout and low-frequency noise. The 1-GHz oscillator-based MIR detector shows a relative frequency deviation of 5.24 × 10^{-10} $Hz^{-1/2}$ at an integration time of 50 μs, leading to an incident noise equivalent power of 197 pW $Hz^{-1/2}$ when input 6-μm MIR light is modulated at 1.8 kHz, and a large dynamic range of 10^7 in incident MIR power. The device architecture is compatible with the scalable manufacturing process and can be readily extended to a broader spectral range by tailoring the absorbing wavelengths of metasurface absorbers.

1. Introduction

Detection of mid-infrared (MIR) radiation, 3 to 50 μm wavelength,[1] is the cornerstone of MIR applications including astronomy,[2] chemical analysis,[3,4] biomedicine,[5,6] agriculture,[7] and communications.[8] A desirable MIR detector would feature high sensitivity, fast response, a large dynamic range, room temperature operation, and a widely designable wavelength range. MIR detectors have been developed based on semiconductor photodiodes, bolometers, nonlinear optics, and mechanical resonators. Semiconductor MIR photodetectors based on mercury cadmium telluride (MCT),[9,10] indium antimonide and aluminum indium arsenide antimonide (InSb/AlInAsSb) material systems,[11–13] quantum well structures,[14,15] and 2D materials,[16–20] have been demonstrated with high responsivity and speed, yet they usually

Z. Xi, J. G. Thomas, J. Ji, Y. Zhu, L. Shao
Bradley Department of Electrical and Computer Engineering
Virginia Tech
Blacksburg, VA 24061, USA
E-mail: shaolb@vt.edu

Z. Cen, D. Wang, J. Zuo, Y. Yao
School of Electrical, Computer and Energy Engineering
Center for Photonic Innovation
Arizona State University
Tempe, AZ 85281, USA
E-mail: yuyao@asu.edu

The ORCID identification number(s) for the author(s) of this article can be found under https://doi.org/10.1002/lpor.202500498

DOI: 10.1002/lpor.202500498

J. G. Thomas, Y. Zhu
Center for Photonics Technology
Virginia Tech
Blacksburg, VA 24061, USA

B. R. Srijanto, I. I. Kravchenko
Center for Nanophase Materials Sciences
Oak Ridge National Laboratory
Oak Ridge, TN 37830, USA

H. Liu
Department of Mathematics
Virginia Tech
Blacksburg, VA 24061, USA

L. Shao
Department of Physics and Center for Quantum Information Science and Engineering (VTQ)
Virginia Tech
Blacksburg, VA 24061, USA

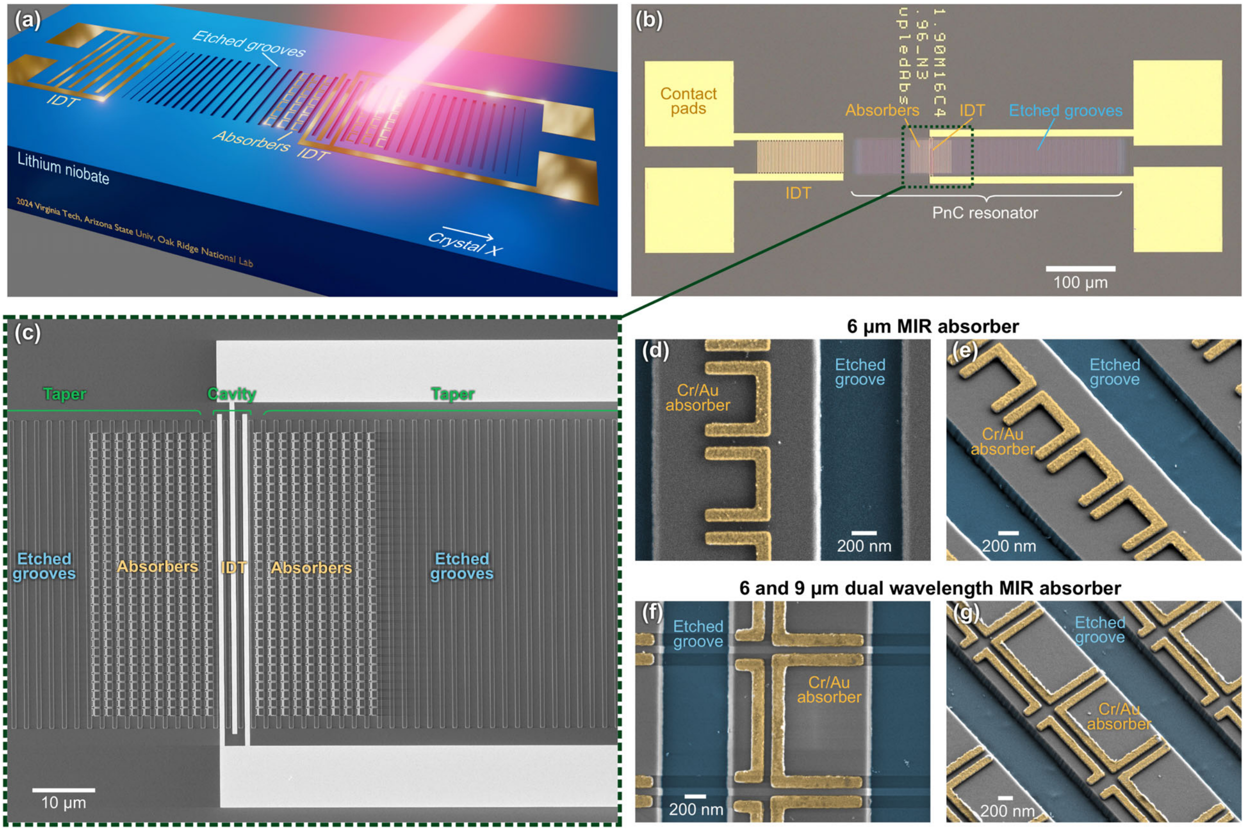

Figure 1. PnC MIR detector. a) Illustration of the detector fabricated on a 128° Y cut LN platform, composed of a PnC resonator defined by etched grooves, a pair of IDT, and an MIR absorber array. IDTs are employed to excite and receive the acoustic wave. The oscillation is formed with sufficient gain provided by a low-noise amplifier. The device is fabricated on 128° Y cut LN with acoustic waves propagating in crystal X direction. b) Microscope image of fabricated detector. IDT and absorbers are made of 10/30 nm Chromium/gold. c) Scanning electron microscopy (SEM) image of the PnC resonator with the absorber array. IDT electrodes and absorbers are placed between the etched grooves in the PnC cavity and taper region. False colored SEM images of d,e) the 6-μm single-wavelength absorbers and f,g) the 6/9-μm dual-wavelength absorbers.

require cryogenic temperatures to achieve high sensitivity due to small photon energy at MIR wavelengths. Moreover, their operation wavelength range is limited by the semiconductor bandgap[9–13] or band offset,[14,15] and the detection sensitivity drops significantly for wavelengths in the long-wave infrared spectral range and beyond (>8 μm). Nonlinear optical approaches[21–27] that up-convert MIR to near infrared or visible can leverage high-performance photodiodes or image sensors at shorter wavelengths, although achieving a high nonlinear conversion efficiency is still challenging on chip. Bolometers based on 2D materials[28,29] and semiconductors[30] demonstrate room-temperature MIR detection yet are still limited by high noise levels and low sensitivity at room temperature.

Compared to photodetectors and bolometers, mechanical resonator-based MIR detectors show advantages in room-temperature MIR detection, especially at wavelengths longer than 5 μm.[31–33] As a temperature-based approach, such mechanical detectors could cover a broad range of wavelengths, either using broadband absorbers, such as platinum thin films,[34] or metamaterial optical absorbers.[35] To date, most mechanical-based MIR detectors leverage suspended mechanical resonators with narrow and long supports tethers (for example, 5-μm wide and 600-μm long tethers in ref. [31]) for high mechanical quality factors and ultimate thermal isolations, resulting in ultrahigh responsivities in relative frequency shift (11000 W^{-1} ref. [31]). However, such tethered structures result in relatively slow thermal response time of a few milliseconds and post challenges for scalable manufacturing and applications in harsh environments, such as under high accelerations.

Here, we demonstrate MIR detectors leveraging low-noise surface acoustic wave phononic crystal (PnC) oscillator on bulk lithium niobate (LN) with co-designed wavelength-and-polarization-selective metamaterial absorbers. The oscillation configuration of our detector enables a direct and large-bandwidth readout of the resonant frequency, as well as reduces the frequency noises by over two orders of magnitude compared to a passive measurement configuration. Our oscillator-based MIR detector features an effective area, defined by its acoustic-wave mode area, of 332 μm^2 and a low relative frequency noise of 5.24×10^{-10} $Hz^{-1/2}$ at an integration time of 50 μs at its oscillation frequency of 1 GHz. The metamaterial absorbers integrated on our PnC resonator offer wavelength and polarization selective MIR absorption. We demonstrate an incident noise equivalent power (NEP) of 197 $pWHz^{-1/2}$ when an input 6-μm MIR light is modulated at 1.8 kHz. Our detector features a large dynamic

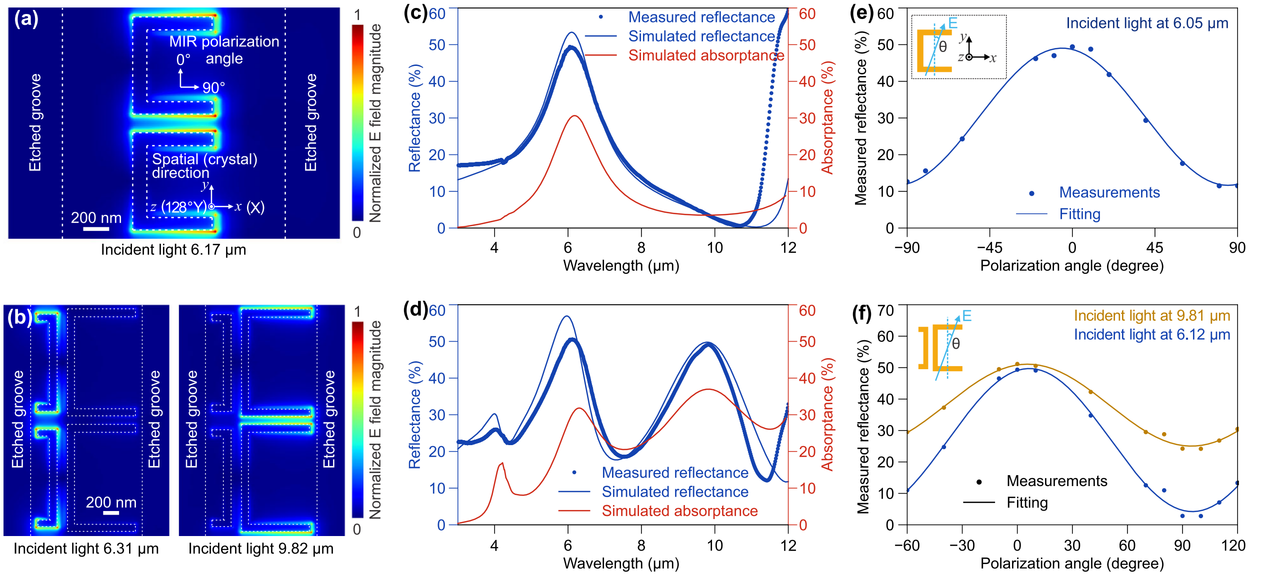

Figure 2. MIR absorbers for 6 µm single wavelength and 6-and-9 µm dual wavelengths. a,b) Numerically simulated near field magnitude distribution at the peak absorption wavelengths. The boundary of the metal absorber and PnC etched grooves is marked by the dashed lines. c,d) Simulated reflection and absorption spectra and experimentally measured reflection spectra. e,f) Experimentally measured polarization-dependent reflection at peak absorption wavelengths. The measured results are fitted to a sine curve. Solid lines represent fitted curves, and dots indicate measured data. The insets illustrate the definition of polarization angle θ, which is the angle between the incident electric field vector E (blue solid arrow) and the antenna axis (blue dashed line). The propagation direction of incident light is normal to the x–y plane. a,c,e) are of the 6-µm single-wavelength absorbers, and b,d,f) are of the 6/9-µm dual-wavelength absorbers.

range of 10^7 in incident MIR power from 100s pW to over 1 mW. By changing the absorber designs, our device architecture could potentially enable monolithic integration of detectors for the full optical spectrum from ultraviolet, to far infrared, and THz waves on a single chip.

2. Metasurface-Absorber-Integrated PnC Resonator for MIR Detection

We develop PnC resonator integrated with metasurface absorbers for MIR detection (**Figure** 1a–c). Our PnC resonator is defined by etched grooves with varying periods and widths in different segments.[36,37] Two interdigital transducers (IDTs) – one located outside, and the other located inside the PnC resonator – provide efficient electromechanical coupling to our PnC resonator. Metasurface absorbers based on coupled plasmonic antennas are placed between the etched grooves at the resonant mode area. The incident MIR is transduced into heat by the absorbers, induces local temperature change, and results in the frequency shift of our PnC resonator via the temperature-dependent elasticity and thermal expansion. As proof of concept, we demonstrate one single-wavelength absorber design for 6 µm wavelength (Figure 1d,e), and another dual-wavelength absorber design for 6 and 9 µm (Figure 1f,g). Our absorbers are made of a thin metal stack of 10-nm-thick chromium and 30-nm-thick gold. We note that a small absorber area is preferred to minimize the mass loading on the PnC structures and the resistive electric loss to the mechanical mode due to the piezoelectric effect of the LN substrate.

We numerically and experimentally characterize the absorbers (**Figure** 2). The 6 µm absorbers employ a C-shape design. At the peak absorption wavelength, the simulated profile shows an enhanced optical electric field in the gap between the C-shape arms (Figure 2a). At the favorable 0° polarization, the numerical simulation shows a reflection peak of 53% at 6.10 µm and an absorption peak of 30% at 6.17 µm (Figure 2c). The experimentally measured reflection spectrum of the 6-µm absorber array shows a peak of 49% at 6.05 µm (Figure 2c), agreeing with our simulation. The measured reflectance at different polarization angles shows a contrast of 5 between the favorable 0° polarization and insensitive 90° polarization (Figure 2e).

The 6-and-9-µm dual-wavelength absorbers employ a double C-shape design. A 6.31-µm incident MIR is resonant with the left narrower C-shape plasmonic antenna, while a 9.81-µm incident MIR is resonant with the right larger C-shape plasmonic antenna (Figure 2b). At the favorable 0° polarization, the simulated reflection spectrum shows peaks of 57% and 50% at 5.97 and 9.77 µm wavelengths, respectively; the simulated absorption spectrum shows peaks of 32% and 37% at 6.31 and 9.82 µm, respectively (Figure 2d). The experimentally measured reflection spectrum shows a peak of 51% and 49% at 6.12 and 9.81 µm, respectively, agreeing with our simulation. The measured reflectance at different polarization angles shows a contrast of 10 at 6.12 µm and a lower contrast of 2 at 9.81 µm due to the higher absorption of LN substrate at this wavelength (Figure 2f). Details of our absorber designs and simulations are provided in Supplemental Note 1.

3. Oscillator Based on PnC Resonator for MIR Detection

Our PnC resonators[36,37] are fabricated on a 128°Y-cut LN substrate with acoustic waves propagating along crystal X axis. This

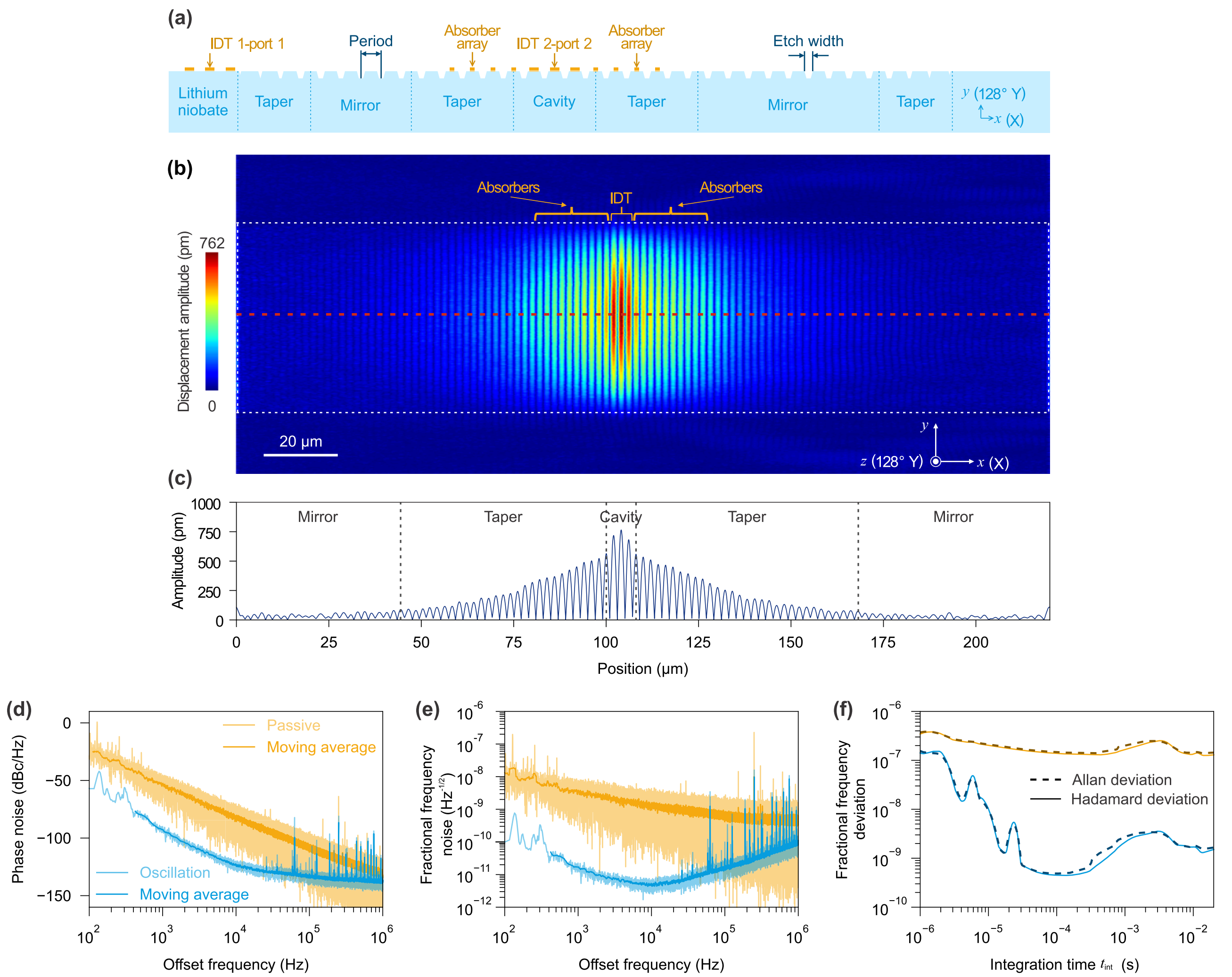

Figure 3. Design and characterization of the PnC resonant mode for MIR detection. a) Cross-section schematic of PnC resonator. The PnC resonator is formed by a cavity segment sandwiched by two mirror segments with taper segments linking them. Grooves in cavity (mirrors) segments are with a spacing period of 2 µm (1.96 µm). The spacing period of etched grooves is quadratically tapering from the cavity segment to the mirror segment. Mirrors transit to the unetched flat segments by linearly tapering the etch width. b) Optically measured displacement field profile of the PnC mode. The color indicates displacement perpendicular to the device surface. The PnC mode is excited by applying a continuous wave at the PnC-resonator-mode frequency applied at IDT 2. c) The cross-section of the displacement profile, indicated by the red dash line in (b). d) Phase noise, e) fractional frequency noise, f) frequency deviation of our PnC resonator in the oscillation and passive measurement configurations. We use the definitions of Allan and Hadamard deviations such that white frequency noise has same deviation values.

128°Y–X configuration offers a low propagation loss, small divergence, and efficient electromechanical coupling for the acoustic waves. The temperature coefficient for the phase velocity of the 128Y-X acoustic waves is –71.2 ppm K^{-1}.[37,38] It is greater than the coefficients of silicon (–60 ppm K^{-1})[33] and silicon nitride (–30 ppm K^{-1}),[31] both are widely used in trampoline detectors. We design the PnC resonator by adjusting periods and widths for etched grooves in different segments (**Figure** 3a). The etched grooves with a period of 1.96 µm in the mirror segments gradually increase to 2.00 µm in the cavity segment. Details of the PnC resonator design are provided in Figure S1 (Supporting Information). The PnC resonator supports a mode at 1 GHz with a loaded Q factor of 1000, leading to a fQ product of 10^{12}, and an electrical transmission (IDT1 to IDT2) of –28 dB (Figure S2b,c, Supporting Information). We measure the acoustic mode profile (Figure 3b,c) using our home-built optical vibrometer.[] The acoustic resonant mode shows a mode area of 332 µm^2 (Supplemental Note 2, Supporting Information).

We employ an oscillation configuration (Figure S3b, Supporting Information) to enable a direct and large-bandwidth readout of the PnC resonator frequency. The oscillation loop consists of our PnC resonator, a low noise amplifier, a phase shifter, and a coupler. The output of our oscillator is first down-converted by an in-phase/quadrature (I/Q) demodulator and then captured by an oscilloscope. Ensuring the accessibility for readers from different fields, we provide phase noise spectrum (Figure 3d), fractional frequency noise spectrum (Figure 3f), and Hadamard deviation (Figure 3g) based on the same measured I/Q data. Our MIR detector oscillating at 1 GHz achieves a minimum fractional frequency noise of 4.32×10^{-12} Hz$^{-1/2}$ at

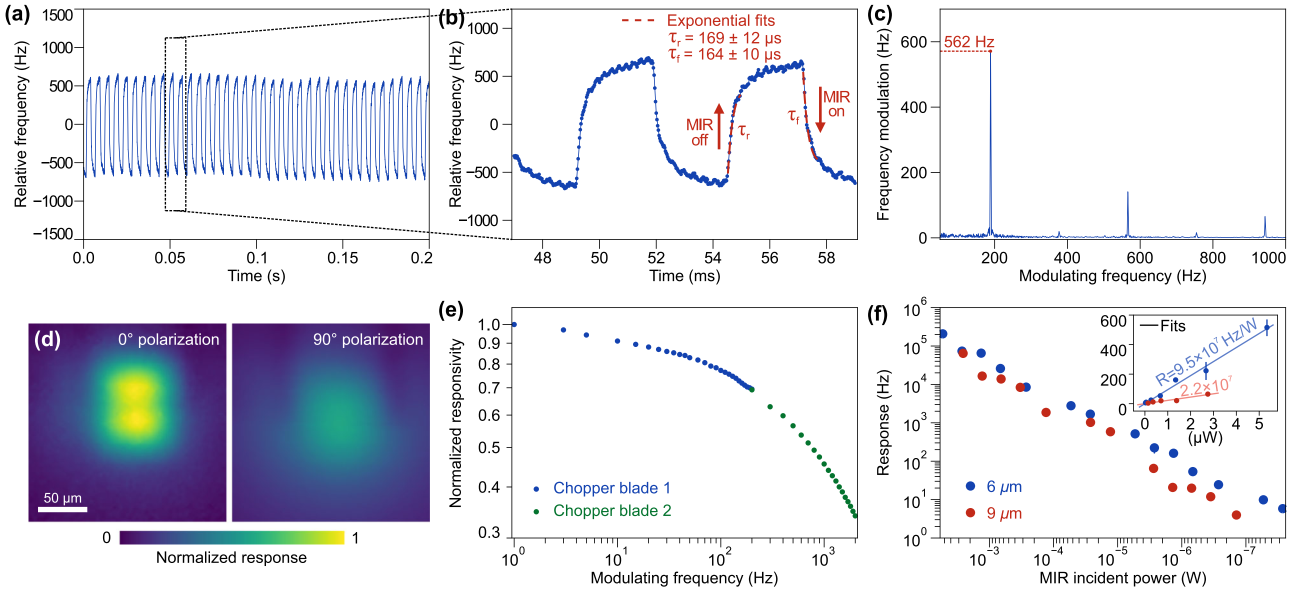

Figure 4. Characterization of our MIR detector with dual-wavelength absorbers. a) Measured modulation of oscillator frequency in response to a chopped MIR input. The incident MIR on the detector is with an average power of 5.3 μW chopped at 190 Hz. b) Zoom in view of (a) showing the detector response time constants of 164 μs in when MIR input is turning on and 169 μs when turning off. c) Frequency spectrum of the frequency modulation signal, showing a peak of 562 at 190 Hz chopper frequency. d) Response mapping of our detector to 0 and 90° polarized MIR input at 6.3 μm. The mapping result is the convolution of the incident MIR beam with the effective area of our detector. e) Frequency response of our detector at MIR incident power of 53.0 μW. Two chopper blades with different opening densities are used to cover the frequency range. 6-μm MIR light is used in (a–e). f) Power-dependent response of our detector at 6 and 9 μm wavelengths. The incident MIR is modulated at 190 Hz. Inset: power-dependent response in linear scale, and the linear fitting shows the responsivities of our detector.

offset frequency of 8,500 Hz, a minimum $\sigma\sqrt{t_{int}} = 3.7 \times 10^{-12}$ given by the frequency deviation σ of 5.24×10^{-10} at integration time t_{int} of 5.0×10^{-5} s. Compared to passive measurement (Figure S3b, Supporting Information), the oscillation configuration reduces the frequency noises by over two orders of magnitude (Figure 3e,f). We note that similar observations showing the advantage of the oscillation configuration have been reported.[40]

We attribute the ultralow-frequency noise of our device for a few reasons. First, the surface acoustic wave (SAW)-based mechanical resonator is constructed on a bulk substrate, which has a much greater thermal conductivity than tethered (suspended) thin-film micromechanical resonators, leading to lower temperature fluctuation noise. Secondly, our design of PnC resonator defined by etched grooves[36,37] enables a higher fQ product than a typical suspended mechanical resonator or metal-defined SAW resonators. Additionally, the strong piezoelectricity of LN allows efficient coupling between mechanical and electrical fields, leading to a lower insertion of the oscillation loop and thus a lower noise. Focused discussion on the noise performance of the PnC oscillator is available in our previous work.[37]

4. Characterization of MIR Detection

We characterize responsivity, bandwidth, and effective areas of our oscillator-based MIR detector. Our experimental setup is shown in Figure S4 (Supporting Information). The results of our devices with 6-and-9-μm dual-wavelength absorbers are shown in **Figure 4**, while the results of our device with 6-μm single-wavelength absorbers are shown in Figure S5 (Supporting Information). We use a quantum cascade laser at 6.30 μm and a distributed feedback laser at 9.55 μm as MIR inputs. The MIR inputs are modulated by a mechanical chopper with variable chopping frequency. The incident MIR power is calibrated to the power within the device area with absorbers (Supplemental Note 3, Supporting Information).

When a 190-Hz-chopped 5.3-μW-power MIR beam at 6.30 μm wavelength is applied on our detector, we observe a frequency modulation of our oscillator-based detector (Figure 4a). As LN has a negative temperature coefficient in elasticity, the oscillating frequency will reduce when light is on the detector. Our detector shows a time constant of 169 (164) μs in the frequency rise (fall) in response to the MIR light off (on) (Figure 4b). By Fourier transform, we see the oscillating frequency of our detectors modulated at the chopper frequency and its higher-order harmonics (Figure 4c). Within this work, we define the response of our detector by the frequency modulation amplitude at the fundamental chopper frequency. For example, a frequency modulation 562 Hz induced by the MIR input of 5.3 μW (Figure 4c).

We map the response at different positions of our detector (Figure 4d). We note that the mapping result is the convolution of the incident MIR beam with the effective area of our detector. Our detector shows a clear polarization-dependent response. For incident light with polarization angle at 0° with respect to the antenna axis, the optical absorption of the antenna metasurface and LN beneath the antenna is enhanced near antenna resonance wavelengths; while for incident light with polarization angle at 90°, the optical absorption is mostly due to LN material

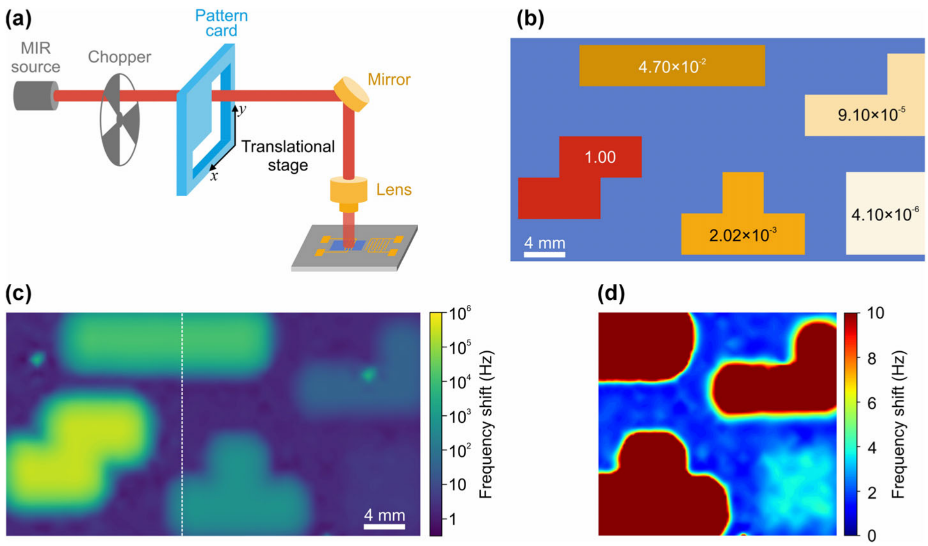

Figure 5. Scanning imaging of Tetris patterns with orders-of-magnitude difference in MIR power. a) Illustration of the scanning imaging setup. b) Tetris patterns with different transmissions. The pattern is prepared by a 3D printed frame covered with glass as attenuators. Transmissions are marked at each opening. c) Scanning image of the patterns. The colors show the induced frequency shift of our detector in the log scale. Dashed lines indicate the stitching of two scans due to the moving range of the translational stage. d) Scanning image of the pattern plotted in the linear scale. The data in (c) and (d) are identical but plotted in different scales. The incident MIR is at 6.3 µm and 3.28 mW at detector without attenuation.

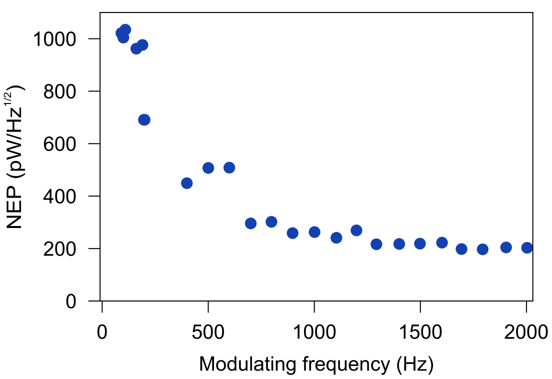

Figure 6. Frequency-dependent noise equivalent power (NEP) of our mid-infrared detector at 6.3 µm wavelength.

absorption in the MIR spectral region. The measurement results confirmed an up to 250% enhancement of infrared detection with antenna absorbers at 6.30 µm, which is around the 6 µm antenna resonance wavelength. As one of the IDTs is placed at the center of the acoustic resonator for optimized electromechanical coupling, the response is slightly lower at the center of the detector. This issue could be addressed by future designs that combine IDT electrodes and absorbers.

We characterize the frequency response of our detector by varying the chopper frequency (Figure 4e). We measure a relative response of 0.77 at 100 Hz, 0.7 at 190 Hz, and 0.46 at 1 kHz, showing a frequency roll-off rate of 4.5 dB per decade. The frequency response is limited by the thermal dynamics of our detector. We note that the frequency roll-off of our detectors is much slower than the 20 dB per decade of RC-limited detectors. Therefore, the relationship between the fitted time constant and bandwidth is different from RC-limited detectors as well.

We test our detector over a large input power range up to 5.3 mW at 6.3 µm wavelength and 2.6 mW at 9 µm wavelength (Figure 4f). Our detector features a large dynamic range of 10^7, from its NEP of 197 pW/$\sqrt{\text{Hz}}$ (see discussion in Section. 5) to 5.3 mW. We note that the maximum tested input power is limited by our MIR laser source and does not imply a device damage threshold. By fitting the measured responses at different incident MIR powers (inset of Figure 4f), we extract a responsivity $R_{190\text{Hz}} = 9.5 \times 10^7$ Hz W^{-1} at 6.3 µm MIR wavelength and 2.2×10^7 Hz W^{-1} at 9 µm wavelength, both at input modulating (chopper) frequency of 190 Hz. At near-DC modulating frequency, the responsivity $R_{\text{DC}} = 1.36 \times 10^8$ and 3.14×10^7 Hz W^{-1} for 6.3 and 9 µm, respectively.

The detector with 6-µm single-wavelength absorbers shows similar performance (Figure S5). The responsivity $R_{190\text{Hz}} = 9.6 \times 10^7$ Hz W^{-1} at input modulating frequency of 190 Hz, and responsivity $R_{\text{DC}} = 1.37 \times 10^8$ Hz W^{-1} at near DC. Compared to near-DC (1 Hz) response, the relative response is 0.79 at 100 Hz, and 0.48 at 1 kHz modulating frequency. These results infer the compatibility of our device architecture with versatile absorbers for different wavelengths.

To demonstrate an application of the large dynamic range, we perform a scanning imaging of Tetris pattern using our detector (**Figure 5**). The Tetris pattern card is mounted on a translational stage with a 3.28-mW 6.3-µm MIR laser as a light source (Figure 5a). Using glass as attenuator, the transmission of Tetris patterns varies about six orders of magnitude from 4.1×10^{-6} (bottom-right "O" Tetris piece) to 1 (bottom-left "S" Tetris piece) (Figure 5b). The scanning results (Figure 5c,d) clearly show the induced oscillation frequency shifts, ranging from 3 Hz to 266 kHz, at different patterns. The spatial resolution of our scanning image is limited by the spot size at the pattern card, which is about 2 millimeters in diameter.

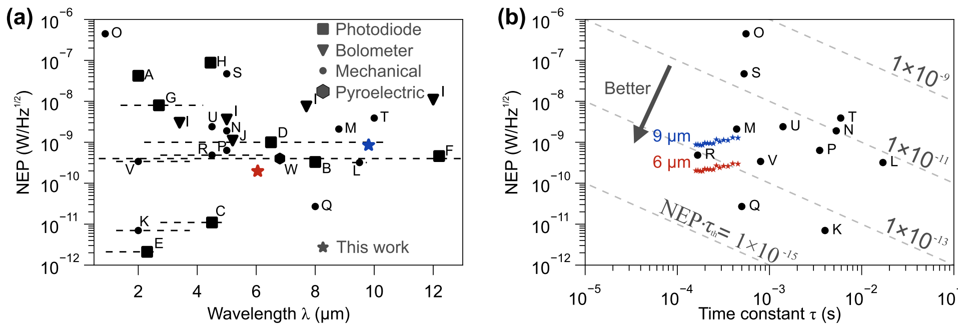

Figure 7. Figure of merits for MIR detectors. a) NEP versus detection wavelengths among photodiodes, bolometers, and mechanical resonators. The plots show the experimentally demonstrated results. If a broadband thermal source is used, the peak detection wavelength is determined by the source temperature or the fiber/filters used. Dashed lines indicate the operation wavelength range, if data is available. b) NEP versus detector time constant among mechanical-based MIR detectors. Labels in the figure: A,[11] B: Thorlabs, VML8T0,[41] C: Thorlabs, VL5T0,[42] D: Thorlabs, VML10T0,[43] E: Thorlabs, PDA10DT,[44] F,[45] G,[20] H,[16] I,[28] J,[29] K,[31] L,[46] M,[47] N,[48] O,[49] P,[50] Q,[33] R,[51] S,[52] T,[53] U,[54] V,[55] W: Laser Components, RP NO1.[56] When frequency-dependent NEP data is not available for previous works or products, a noise-floor-limited NEP $= f_0\sigma\sqrt{t_{int}}/R_{DC}$ was used, which could overestimate the performance.

5. Noise Equivalent Power and Comparison

The frequency-dependent NEP of a detector can be given by $f_0\sqrt{S_y(f)}/R(f)$, where $S_y(f)$ in Hz^{-1} is the power spectral density of fractional frequency noise, f_0 is oscillation frequency, and $R(f)$ in Hz/W is the responsivity at input frequency of f. By this definition, we extract the frequency-dependent NEP (**Figure 6**) using the frequency noise in Figure 3e and frequency-dependent response in Figure 4e. With respect to the incident light on the detector effective area, our dual-wavelength detector features a minimum NEP of 197 pW $\text{Hz}^{-1/2}$ at input frequency of 1.8 kHz at 6.3 µm input wavelength. At low input modulating frequencies (below 500 Hz), the NEP is limited by the larger frequency noise in long time scale. At the input frequency within the range of 700 Hz to 2 kHz, the NEP is almost flat, since both the responsivity and the frequency noise reduce with increasing frequency. On the other hand, if we define the detection bandwidth by the frequency-dependent NEP, our detector shows a bandwidth of at least 2 kHz.

Figure 7 summarizes the performance of MIR detectors at room temperature; incident powers are calculated using MIR power on the detector effective area. While MIR photodiodes have demonstrated large bandwidths of 7 GHz based on semiconductor[11] and 500 GHz based on 2D materials,[20] the mechanical resonator-based approaches show advantages in lower NEP at longer MIR wavelengths (Figure 7a). Among mechanical-resonator-based detectors, our fully supported detectors show competitive NEP and time constants, leading to a competitive figure-of-merit, NEP· τ (Figure 7b; Table S1, Supporting Information). We note that due to the availability of data in previous works and products, they are used in this comparison.

We model the dynamics of our oscillator-based MIR detector by its thermodynamics and mechanical oscillation (Supplemental Note 4, Supporting Information). The temperature change of the resonator induced by the MIR absorption is parametrically coupled to the resonant frequency of the mechanical resonator. The thermodynamics limits the detector response time. Thermodynamic bandwidth could be further improved by employing thin-film LN on sapphire.[57] We consider two main noise sources of our oscillator-based MIR detector: temperature fluctuation noise of the mechanical resonator and the thermal noise in the oscillation loop. The temperature fluctuation noise is considered a fundamental limit for mechanical-resonator-based MIR detection, which imposes a NEP of 4.38 pW $\text{Hz}^{-1/2}$ for our devices, which could be improved by employing a smaller resonator. The thermal noise in the oscillation loop that amplified by the low-noise amplifier imposes a NEP of 0.62 pW $\text{Hz}^{-1/2}$. Thus, the temperature fluctuation noise is the dominating noise of our detectors. We note that the NEP from the theoretical model is lower than our experimental demonstration, and we speculate a few possible reasons for the mismatch. (1) The low noise amplifier is working in the saturation region for our oscillation detector, leading to a higher noise factor, and (2) the rate equations in our toy model may be oversimplified to describe the nonlinear dynamics and noise performance. Despite such mismatch, our analytical solutions and simulations can still provide insights into future developments. Looking into the future, a higher Q factor, a lower insertion loss, or a higher power level in the oscillation loop could further improve the NEP.

6. Conclusion and Outlook

Our mechanical-oscillator-based MIR detectors feature ultra-low noise, high sensitivity, fast response, and large dynamic ranges without any cooling at room temperature. Compared to passive readout approaches, the oscillation configuration of our detector enables an ultralow frequency noise in reading out the resonant frequency. Integrating plasmonic antennas metasurface absorbers with these microscale MIR detectors/detector arrays could provide versatile, compact and high speed solutions for single or multi-wavelength, spectroscopic and polarization detection over the whole infrared wavelength range, which find various applications in vibrational spectroscopy,[58] infrared polarimetry,[59,60] remote sensing,[61–63] chemical analysis,[64,65] and biomedical diagnosis.[66] With flexible absorber designs, our MIR detector architecture can also enable monolithic solutions for ultraviolet to far infrared applications. Moreover, its fabrication process is compatible with recently established LN foundries and scalable at wafer scale.[67] For integrated platforms, the PnC resonators can be integrated with optical waveguides[68] enabling sensitive detection for MIR photonic integrated circuits.

Supporting Information

Supporting Information is available from the Wiley Online Library or from the author.

Acknowledgements

Z.X., Z.C., and D.W. contributed equally to this work. Device fabrication was conducted as part of user projects at the Center for Nanophase Materials Sciences (CNMS), which is a DOE Office of Science User Facility. This work was supported by the Defense Advanced Research Projects Agency (DARPA) OPTIM program. The views and conclusions contained in this document are those of the authors and do not necessarily reflect the position or the policy of the Government. No official endorsement should be inferred. Approved for public release; distribution is unlimited. DOE Office of Science User Facility (CNMS2022-B-01473, CNMS2024-B-02643); Defense Advanced Research Projects Agency (DARPA) (HR00112320031).

Conflict of Interest

Virginia Tech and Arizona State University has filed a provisional application for patent related to this work. The authors declare no other competing interests.

Data availability statement

Data that supports the findings of this study are available from the corresponding authors upon reasonable request.

Keywords

mechanical oscillator, metasurface absorber, mid-infrared detection, phononic crystal

Received: March 5, 2025
Revised: June 19, 2025
Published online:

[1] ISO 20473:2007, Optics and photonics – Spectral bands.
[2] S. F. Hönig, M. Kishimoto, P. Gandhi, A. Smette, D. Asmus, W. Duschl, M. Polletta, G. Weigelt, *Astron. Astrophys.* **2010**, *515*, A23.
[3] M. Yu, Y. Okawachi, A. G. Griffith, N. Picqué, M. Lipson, A. L. Gaeta, *Nat. Commun.* **2018**, *9*, 1869.
[4] M. Liu, R. M. Gray, L. Costa, C. R. Markus, A. Roy, A. Marandi, *Nat. Commun.* **2023**, *14*, 1044.
[5] E. F. J. Ring, K. Ammer, *Physiol. Meas.* **2012**, *33*, R33.
[6] D. Rodrigo, O. Limaj, D. Janner, D. Etezadi, F. J. García de Abajo, V. Pruneri, H. Altug, *Science* **2015**, *349*, 165.
[7] R. Ishimwe, K. Abutaleb, F. Ahmed, *Adv. Remote Sens.* **2014**, *3*, 128.
[8] X. Pang, O. Ozolins, S. Jia, L. Zhang, R. Schatz, A. Udalcovs, V. Bobrovs, H. Hu, T. Morioka, Y.-T. Sun, J. Chen, S. Lourdudoss, L. K. Oxenløwe, S. Popov, X. Yu, *J. Lightwave Technol.* **2022**, *40*, 3149.
[9] P. D. Anderson, J. D. Beck, W. Sullivan, C. Schaake, J. McCurdy, M. Skokan, P. Mitra, X. Sun, *J. Electron. Mater.* **2022**, *51*, 6803.
[10] J. Beck, C. Wan, M. Kinch, J. Robinson, P. Mitra, R. Scritchfield, F. Ma, J. Campbell, *J. Electron. Mater.* **2006**, *35*, 1166.
[11] D. Chen, S. D. March, A. H. Jones, Y. Shen, A. A. Dadey, K. Sun, J. A. McArthur, A. M. Skipper, X. Xue, B. Guo, J. Bai, S. R. Bank, J. C. Campbell, *Nat. Photonics* **2023**, *17*, 594.
[12] A. H. Jones, S. D. March, S. R. Bank, J. C. Campbell, *Nat. Photonics* **2020**, *14*, 559.
[13] C. Xie, M. Aziz, V. Pusino, A. Khalid, M. Steer, I. G. Thayne, M. Sorel, D. R. S. Cumming, *Optica* **2017**, *4*, 1498.
[14] A. Delga, in *Mid-infrared Optoelectronics*, (Eds.: E. Tournié, L. Cerutti), Woodhead Publishing, Duxford, United Kingdom, **2020**.
[15] B. F. Levine, *J. Appl. Phys.* **1993**, *74*, 5476.
[16] Y. Yao, R. Shankar, P. Rauter, Y. Song, J. Kong, M. Loncar, F. Capasso, *Nano Lett.* **2014**, *14*, 3749.
[17] Q. Guo, A. Pospischil, M. Bhuiyan, H. Jiang, H. Tian, D. Farmer, B. Deng, C. Li, S.-J. Han, H. Wang, Q. Xia, T.-P. Ma, T. Mueller, F. Xia, *Nano Lett.* **2016**, *16*, 4648.
[18] X. Chen, X. Lu, B. Deng, O. Sinai, Y. Shao, C. Li, S. Yuan, V. Tran, K. Watanabe, T. Taniguchi, D. Naveh, L. Yang, F. Xia, *Nat. Commun.* **2017**, *8*, 1672.
[19] Y. Fang, Y. Ge, C. Wang, H. Zhang, *Laser Photonics Rev.* **2020**, *14*, 1900098.
[20] S. M. Koepfli, M. Baumann, Y. Koyaz, R. Gadola, A. Güngör, K. Keller, Y. Horst, S. Nashashibi, R. Schwanninger, M. Doderer, E. Passerini, Y. Fedoryshyn, J. Leuthold, *Science* **2023**, *380*, 1169.
[21] S. M. M. Friis, L. Høgstedt, *Opt. Lett.* **2019**, *44*, 4231.
[22] T. W. Neely, L. Nugent-Glandorf, F. Adler, S. A. Diddams, *Opt. Lett.* **2012**, *37*, 4332.
[23] P. J. Rodrigo, L. Høgstedt, S. M. M. Friis, L. R. Lindvold, P. Tidemand-Lichtenberg, C. Pedersen, *Laser Photonics Rev.* **2021**, *15*, 2000443.
[24] S. Wolf, J. Kiessling, M. Kunz, G. Popko, K. Buse, F. Kühnemann, *Opt. Express* **2017**, *25*, 14504.
[25] P. Tidemand-Lichtenberg, J. S. Dam, H. V. Andersen, L. Høgstedt, C. Pedersen, *J. Opt. Soc. Am. B* **2016**, *33*, D28.
[26] Y. Cai, Y. Chen, X. Xin, K. Huang, E. Wu, *Photonis Res.* **2022**, 10.
[27] J. Fang, K. Huang, R. Qin, Y. Liang, E. Wu, M. Yan, H. Zeng, *Nat. Commun.* **2024**, *15*, 1811.
[28] S. Yuan, R. Yu, C. Ma, B. Deng, Q. Guo, X. Chen, C. Li, C. Chen, K. Watanabe, T. Taniguchi, F. J. García de Abajo, F. Xia, *ACS Photonics* **2020**, *7*, 1206.
[29] J. Goldstein, H. Lin, S. Deckoff-Jones, M. Hempel, A.-Y. Lu, K. A. Richardson, T. Palacios, J. Kong, J. Hu, D. Englund, *Nat. Commun.* **2022**, *13*, 3915.
[30] J. Shim, J. Lim, I. Kim, J. Jeong, B. H. Kim, S. K. Kim, D.-M. Geum, S. Kim, *arXiv e-prints* **2024**, 2405.14155.
[31] M. Piller, J. Hiesberger, E. Wistrela, P. Martini, N. Luhmann, S. Schmid, *IEEE Sens. J.* **2023**, *23*, 1066.
[32] M. E. Gülseren, M. Benson, R. W. Parker, J. Segovia-Fernandez, E. T. T. Yen, J. S. Gómez-Díaz, *IEEE Sens. J.* **2024**, *24*, 17313.
[33] L. Laurent, J.-J. Yon, J.-S. Moulet, M. Roukes, L. Duraffourg, *Phys. Rev. Appl.* **2018**, *9*, 024016.
[34] S.-E. Stanca, V. R. Rayapati, A. Chakraborty, J. Dellith, W. Fritzsche, G. Zieger, H. Schmidt, *Sci. Rep.* **2024**, *14*, 22709.
[35] J. A. Bossard, L. Lin, S. Yun, L. Liu, D. H. Werner, T. S. Mayer, *ACS Nano* **2014**, *8*, 1517.
[36] L. Shao, S. Maity, L. Zheng, L. Wu, A. Shams-Ansari, Y.-I. Sohn, E. Puma, M. N. Gadalla, M. Zhang, C. Wang, E. Hu, K. Lai, M. Lončar, *Phys. Rev. Appl.* **2019**, *12*, 014022.
[37] Z. Xi, J. G. Thomas, J. Ji, D. Wang, Z. Cen, I. I. Kravchenko, B. R. Srijanto, Y. Yao, Y. Zhu, L. Shao, *Phys. Rev. Appl.* **2025**, *23*, 024054.
[38] R. B. Ward, *IEEE Trans. Ultrason. Ferroelectr. Freq. Control* **1990**, *37*, 481.

[39] J. G. Thomas, Z. Xi, J. Ji, G. Shi, B. R. Srijanto, I. I. Kravchenko, Y. Yao, L. Shao, Y. Zhu, *Optica* **2025**, *12*, 935.
[40] Y. Huang, J. G. Flor Flores, Y. Li, W. Wang, D. Wang, N. Goldberg, J. Zheng, M. Yu, M. Lu, M. Kutzer, D. Rogers, D.-L. Kwong, L. Churchill, C. W. Wong, *Laser Photonics Rev.* **2020**, *14*, 1800329.
[41] https://www.thorlabs.com/thorproduct.cfm?partnumber=VML8T0.
[42] https://www.thorlabs.com/thorproduct.cfm?partnumber=VL5T0.
[43] https://www.thorlabs.com/thorproduct.cfm?partnumber=VML10T0.
[44] https://www.thorlabs.com/thorproduct.cfm?partnumber=PDA10DT.
[45] Q. Guo, R. Yu, C. Li, S. Yuan, B. Deng, F. J. García de Abajo, F. Xia, *Nat. Mater.* **2018**, *17*, 986.
[46] P. Markus, L. Niklas, C. Miao-Hsuan, S. Silvan, presented at Proc.SPIE **2019**, *11088*, 1108802, https://doi.org/10.1117/12.2528416.
[47] Y. Hui, J. S. Gomez-Diaz, Z. Qian, A. Alù, M. Rinaldi, *Nat. Commun.* **2016**, *7*, 11249.
[48] Y. Hui, S. Kang, Z. Qian, M. Rinaldi, *J. Microelectromech. Syst.* **2021**, *30*, 165.
[49] V. J. Gokhale, M. Rais-Zadeh, *J. Microelectromech. Syst.* **2014**, *23*, 803.
[50] Z. Qian, S. Kang, V. Rajaram, M. Rinaldi, presented at 2016 IEEE Sensors Oct.-Nov. **2016**.
[51] Z. Qian, V. Rajaram, S. Kang, M. Rinaldi, *Appl. Phys. Lett.* **2019**, *115*, 261102.
[52] Z. Qian, Y. Hui, F. Liu, S. Kang, S. Kar, M. Rinaldi, *Microsyst. Nanoeng.* **2016**, *2*, 16026.
[53] M. B. Pisani, K. Ren, P. Kao, S. Tadigadapa, *J. Microelectromech. Syst.* **2011**, *20*, 288.
[54] Y. Hui, M. Rinaldi, presented at *2013 Transducers & Eurosensors XXVII: The 17th International Conference on Solid-State Sensors, Actuators and Microsystems* Barcelona, Spain, Otober **2013**.
[55] W. C. Ang, P. Kropelnicki, H. Campanella, Y. Zhu, A. B. Randles, H. Cai, Y. A. Gu, K. C. Leong, C. S. Tan, presented at *2014 IEEE 27th International Conference on Micro Electro Mechanical Systems (MEMS)* San Francisco, CA, USA Jan. **2014**.
[56] https://www.lasercomponents.com/us/product/pr-series-ir-thz-receivers/.
[57] L. Shao, S. W. Ding, Y. Ma, Y. Zhang, N. Sinclair, M. Lončar, *Phys. Rev. Appl.* **2022**, *18*, 054078.
[58] B. Zheng, H. Zhao, B. Cerjan, S. Yazdi, E. Ringe, P. Nordlander, N. J. Halas, *Appl. Phys. Lett.* **2018**, 113.
[59] M. Dai, C. Wang, B. Qiang, F. Wang, M. Ye, S. Han, Y. Luo, Q. J. Wang, *Nat. Commun.* **2022**, *13*, 4560.
[60] J. Chen, F. Yu, X. Liu, Y. Bao, R. Chen, Z. Zhao, J. Wang, X. Wang, W. Liu, Y. Shi, C.-W. Qiu, X. Chen, W. Lu, G. Li, *Light: Sci. Appl.* **2023**, *12*, 105.
[61] S. Yang, X. Yan, H. Qin, Q. Zeng, Y. Liang, H. Arguello, X. Yuan, *Remote Sens.* **2021**, *13*, 741.
[62] P. Y. Deschamps, F. M. Breon, M. Leroy, A. Podaire, A. Bricaud, J. C. Buriez, G. Seze, *IEEE Trans. Geosci. Remote Sens.* **1994**, *32*, 598.
[63] X. Tan, H. Zhang, J. Li, H. Wan, Q. Guo, H. Zhu, H. Liu, F. Yi, *Nat. Commun.* **2020**, *11*, 5245.
[64] D. Knez, B. W. Toulson, A. Chen, M. H. Ettenberg, H. Nguyen, E. O. Potma, D. A. Fishman, *Sci. Adv.* **2022**, *8*, ade4247.
[65] L. Shi, X. Liu, L. Shi, H. T. Stinson, J. Rowlette, L. J. Kahl, C. R. Evans, C. Zheng, L. E. P. Dietrich, W. Min, *Nat. Methods* **2020**, *17*, 844.
[66] Y. Zhao, S. Kusama, Y. Furutani, W.-H. Huang, C.-W. Luo, T. Fuji, *Nat. Commun.* **2023**, *14*, 3929.
[67] K. Luke, P. Kharel, C. Reimer, L. He, M. Loncar, M. Zhang, *Opt. Express* **2020**, *28*, 24452.
[68] L. Shao, S. W. Ding, N. Sinclair, J. G. Leatham, M. Loncar, presented at Conference on Lasers and Electro-Optics, San Jose, California, May **2022**.